The Astrophysical Journal, 939:15 (11pp), 2022 November 1 https://doi.org/10.3847/1538-4357/ac9306

Comparison of Electron Capture Rates in the $N = 50$ Region using 1D Simulations of Core-collapse Supernovae

Zac Johnston[1,2], Sheldon Wasik[1], Rachel Titus[1,3], MacKenzie L. Warren[1,2,4], Evan P. O'Connor[5], Remco Zegers[1,2,3], and Sean M. Couch[1,2,3,6]
[1] Department of Physics and Astronomy, Michigan State University, East Lansing, MI 48824, USA; zacjohn@msu.edu
[2] Joint Institute for Nuclear Astrophysics–Center for the Evolution of the Elements, Michigan State University, East Lansing, MI 48824, USA
[3] National Superconducting Cyclotron Laboratory, Michigan State University, East Lansing, MI 48824, USA
[4] Department of Physics, North Carolina State University, Raleigh, NC 27695, USA
[5] The Oskar Klein Centre, Department of Astronomy, Stockholm University, AlbaNova, SE-106 91 Stockholm, Sweden
[6] Department of Computational Mathematics, Science, and Engineering, Michigan State University, East Lansing, MI 48824, USA
Received 2022 February 18; revised 2022 September 9; accepted 2022 September 16; published 2022 October 27

Abstract

Recent studies have highlighted the sensitivity of core-collapse supernovae (CCSNe) models to electron-capture (EC) rates on neutron-rich nuclei near the $N = 50$ closed-shell region. In this work, we perform a large suite of one-dimensional CCSN simulations for 200 stellar progenitors using recently updated EC rates in this region. For comparison, we repeat the simulations using two previous implementations of EC rates: a microphysical library with parametrized $N = 50$ rates (LMP), and an older independent-particle approximation (IPA). We follow the simulations through shock revival up to several seconds post-bounce, and show that the EC rates produce a consistent imprint on CCSN properties, often surpassing the role of the progenitor itself. Notable impacts include the timescale of core collapse, the electron fraction and mass of the inner core at bounce, the accretion rate through the shock, the success or failure of revival, and the properties of the central compact remnant. We also compare the observable neutrino signal of the neutronization burst in a DUNE-like detector, and find consistent impacts on the counts and mean energies. Overall, the updated rates result in properties that are intermediate between LMP and IPA, and yet slightly more favorable to explosion than both.

Unified Astronomy Thesaurus concepts: Core-collapse supernovae (304); Supernova neutrinos (1666); Neutrino astronomy (1100); Reaction rates (2081)

1. Introduction

Massive stars ($\gtrsim 8\ M_\odot$) are destined to undergo iron core collapse, either imploding entirely into a black hole (BH), or violently ejecting their outer layers and leaving behind a proto-neutron star (PNS) in a core-collapse supernova (CCSN; see reviews in Janka et al. 2007; Müller 2020). Of the myriad physical processes that contribute to these stellar deaths, the capture of electrons onto protons via the weak interaction plays a central role.

Electron capture (EC) regulates the deleptonization of nuclear matter during collapse, and thus helps to set the initial conditions of the shock at core bounce (see reviews in Langanke & Martínez-Pinedo 2003; Langanke et al. 2021). The uncertainties on EC rates can span orders of magnitude and produce larger variations in core-collapse properties than changes to the nuclear equation of state (EOS) or stellar progenitor (Sullivan et al. 2016; Pascal et al. 2020).

It is experimentally and computationally difficult to constrain EC rates under astrophysical conditions, especially for the heavy, neutron-rich nuclei relevant to core collapse. For this reason, CCSN simulations typically rely on parametrized approximations, particularly those of Bruenn (1985) and Langanke et al. (2003). Recent decades, however, have seen the continued development of tabulated rates for larger numbers of nuclei based on shell-model calculations (e.g., Oda et al. 1994; Langanke & Martınez-Pinedo 2000; Langanke et al. 2003; Suzuki et al. 2016).

A systematic study by Sullivan et al. (2016) showed that core-collapse simulations were most sensitive to changes in the EC rates of neutron-rich nuclei near the $N = 50$, $Z = 28$ closed-shell region. The drawback is that most of these rates relied on the parameterization of Langanke et al. (2003), which is extrapolated from rates on nuclei near the valley of stability. In a follow-up study focusing on 74 nuclei in the high-sensitivity region, Titus et al. (2018) showed that these rates are likely overestimated by up to two orders of magnitude, further emphasizing the need for updated rates. Using new experimental measurements of the ^{86}Kr(t, ^{3}He + γ) charge-exchange reaction, Titus et al. (2019) calculated microphysical rates on 78 nuclei in this region, confirming that the parametrized rates are overestimated.

Raduta et al. (2017) improved upon the parameterization of Langanke et al. (2003) for neutron-rich nuclei by accounting for temperature, electron density, and odd–even effects. Comparing one-dimensional (1D) core-collapse simulations using this improved parameterization, Pascal et al. (2020) demonstrated the expected increase in core mass and electron fraction due to an average decrease in EC rates. Pascal et al. (2020) also performed a rate sensitivity study, independently verifying the findings of Sullivan et al. (2016) and Titus et al. (2018) that EC rates in the $N = 50$ region remain the most crucial for CCSNe.

In this paper, we present simulations of CCSNe through to shock revival/failure for 200 stellar progenitors using the updated $N = 50$ rates from Titus et al. (2019). We run

corresponding simulations using the baseline rate library from Sullivan et al. (2016) with the improved approximation of Raduta et al. (2017), and a third set using the independent-particle approximation (IPA) of Bruenn (1985). By comparing the model sets, we investigate the impact of updated EC rates on core collapse, shock revival, and neutrino emission across a variety of progenitors.

The paper is structured as follows. In Section 2, we describe our methods, including the EC rate tables (Section 2.1), the setup of the CCSN simulations (Section 2.2), and the calculation of observable neutrino signals (Section 2.3). In Section 3, we compare the simulation results, with a detailed comparison of three reference progenitors (Section 3.1), the impact across the full progenitor population (Section 3.2), the compact remnants (Section 3.3), and the predicted neutrino signal (Section 3.4). In Section 4, we interpret our results and compare them to previous studies, and give concluding remarks in Section 5.

2. Methods

To explore the impact of EC rates on CCSNe, we run multiple large sets of 1D simulations using the FLASH code (Fryxell et al. 2000; Dubey et al. 2009). For initial conditions, we use 200 stellar progenitor models from Sukhbold et al. (2016) with zero-age main-sequence (ZAMS) masses between 9 and 120 $M_\odot$ (Section 2.2).

For each progenitor, we run simulations using three different implementations of EC rates, which include an IPA, microphysical calculations, and updated experimental rates (Section 2.1). For the 20 and 40 $M_\odot$ progenitors, we also run simulations with the microphysical rates scaled by factors of 0.01 and 10. In total, this results in 612 supernova models evolved to between 1 and 5 s post-bounce.

2.1. EC Rates

The first of our three EC rate sets uses the IPA on a mean nucleus (Fuller et al. 1982; Bruenn 1985). These rates were used in the comparable FLASH simulations of Couch et al. (2020) and Warren et al. (2020, though see Section 2.2 for a note on differences). Crucially, IPA assumes that EC completely halts for nuclei with $N \geqslant 40$ due to Pauli blocking, thus only permitting captures on free protons at densities above $\sim 10^{10}$ g cm^3, where neutron-rich nuclei dominate the composition (Langanke et al. 2003).

The second set, which we label LMP, uses a library of microphysical rates compiled by the National Superconducting Cyclotron Laboratory (NSCL) Charge-Exchange Group [7,8] (Sullivan et al. 2016; Titus et al. 2018). This library includes rates from Fuller et al. (1982), Oda et al. (1994), Langanke & Martınez-Pinedo (2000), Langanke et al. (2003), Pruet et al. (2003), and Suzuki et al. (2016). For nuclei that are not covered by the above calculations, the single-state parameterization from Raduta et al. (2017, Model 3) is used, which extends the approximation of Langanke et al. (2003) to account for temperature, electron density, and odd–even effects. By unblocking EC on neutron-rich nuclei, these modern calculations replace the assumption in IPA that deleptonization is dominated at high densities by EC on free protons (Langanke et al. 2003).

The third set, which we label LMP+N50, is the same as LMP except for updated microphysical rates in the region around $N = 50$, $Z = 28$, where core collapse is known to be highly sensitive (Sullivan et al. 2016; Titus et al. 2018; Pascal et al. 2020). These new rates were calculated for 78 nuclei by Titus et al. (2019) using a quasi-particle random-phase approximation using constraints from (t, ^{3}He + γ) charge-exchange experiments. The LMP set largely relies on the Raduta et al. (2017) parameterization for these rates, and are up to two orders of magnitude higher than the LMP+N50 set. This is due to the fact that in the LMP+N50 set Pauli-blocking effects that reduce the rates play an important role as only transitions from the ground state are considered (Titus et al. 2018, 2019).

Recently, Dzhioev et al. (2020) argued that Pauli unblocking at finite temperature may actually reduce or eliminate this gap. Indeed, during the latter stages of our present study, Giraud et al. (2022) reported new finite-temperature calculations for the $N = 50$ region, which resulted in rates around an order of magnitude higher than LMP+N50 for $T \lesssim 10GK$ and $\rho Y_e = 10^{11}$ g cm^3. This improvement brings the rates closer to the original LMP approximation, but still lower by about a factor of 5. The calculations by Dzhioev et al. (2020) and Giraud et al. (2022) both indicate that the temperature-dependent effects significantly increase the EC rates compared to those estimated on the basis of captures on the ground state only by Titus et al. (2019). Although a future study will be required to determine the impact of the rates developed in Giraud et al. (2022), we note that the LMP+N50 rates by Titus et al. (2019) should be regarded as lower limits, and on the basis of Giraud et al. (2022), the LMP rates provide a more realistic estimate but are likely still overestimated.

For the 12, 20, and 40 $M_\odot$ progenitors, in addition to the three EC rate sets above, we also systematically scale the rates of LMP and LMP+N50 following the approach used in Sullivan et al. (2016), whereby the rates of all nuclei with atomic mass numbers of $A > 4$ are scaled by factors of 0.01 and 10 (hereafter labeled 0.01× and 10×).

2.2. Numerical Methods

To simulate the collapse and explosion of massive stars, we use the FLASH hydrodynamics code (Fryxell et al. 2000; Dubey et al. 2009) with the Supernova Turbulence in Reduced-dimensionality (STIR) framework (Couch et al. 2020; Warren et al. 2020).

STIR enhances the *explodability* of 1D CCSN models by using time-dependent mixing-length theory to approximate convective turbulence in 1D. We use a mixing length parameter of $\alpha_\Lambda = 1.25$, chosen to reproduce the convective velocities of 3D simulations, which is multiplied by the pressure scale height to obtain the mixing length (for details, see Couch et al. 2020).

We use a recently implemented hydrodynamics solver (Couch et al. 2020), which uses a fifth-order finite-volume weighted essentially non-oscillatory spatial discretization, and a method-of-line Runge–Kutta time integration.

For neutrino transport, we use the "M1" scheme, an explicit two-moment method with an analytic closure (described in O'Connor & Couch 2018), with three neutrino species (ν_e, $\bar{\nu}_e$,

[7] https://github.com/csullivan/weakrates
[8] https://groups.nscl.msu.edu/charge_exchange/weakrates.html

and $\nu_x = \{\nu_\mu, \nu_\tau, \bar{\nu}_\mu, \bar{\nu}_\tau\}$) and 18 logarithmically spaced energy groups between 1 and 300 MeV.

We generate neutrino opacity tables using the open-source neutrino interaction library NULIB[9] (O'Connor 2015). The interaction rates largely follow Bruenn (1985) and Burrows et al. (2006), with corrections for weak magnetism and nucleon recoil from Horowitz (2002). Separate tables are calculated using the neutrino emissivities derived from each EC rate set described in Section 2.1. We note that our tables do not include the many-body effects and virial corrections to neutrino-nucleon scattering from Horowitz et al. (2017). These corrections aid explodability by enhancing neutrino heating in the gain region (O'Connor et al. 2017), and thus our simulations result in fewer explosions than the corresponding models in Couch et al. (2020) and Warren et al. (2020). Nevertheless, this does not impede our goal of a comparison study between the EC rates.

We use the SFHo EOS from Steiner et al. (2013), and assume nuclear statistical equilibrium (NSE) abundances everywhere in the domain. For the IPA EC rates, the average nucleus from the NSE distribution is used. Self-gravity is included using an approximate general-relativistic effective potential (Marek et al. 2006; O'Connor & Couch 2018).

For initial conditions, we use 200 stellar progenitor models from Sukhbold et al. (2016), the same set used with FLASH +STIR in Couch et al. (2020) and Warren et al. (2020). These progenitors are spherically symmetric, solar-metallicity, non-rotating, and nonmagnetic, with ZAMS masses ranging from 9–120 $M_\odot$. The set spans core compactness values of $0 \lesssim \xi_{2.5} \lesssim 0.54$ (as defined in O'Connor & Ott 2011) and iron core masses of $1.29 \lesssim M_{\rm Fe} \lesssim 1.84 M_\odot$.

The simulation domain extends from the center of the star to $r = 15{,}000$ km. The domain is divided into 15 adaptive mesh refinement blocks, each containing 16 zones. We allow up to nine levels of mesh refinement, resulting in a zone resolution of 62.5 km at the coarsest level and 0.244 km at the finest level. The adaptive mesh refinement results in a total of roughly 1000 zones.

2.3. Neutrino Observables

Following the approach used in Warren et al. (2020), we calculate simulated observations of the neutrino burst at core bounce using SNOWGLOBES[10] (Scholberg 2012), which uses the GLOBES[11] (Huber et al. 2005) framework to predict event rates for a given detector material.

As input for SNOWGLOBES, we calculate from our simulations the neutrino flux at Earth assuming a CCSN distance of 10 kpc and a pinched neutrino spectrum with a Fermi–Dirac parameterization (Keil et al. 2003). We include adiabatic neutrino flavor conversions from Mikheyev–Smirnov–Wolfenstein (MSW) matter effects (Dighe & Smirnov 2000). For each model, we apply three separate cases of flavor mixing: no flavor mixing, normal neutrino mass ordering, and inverted mass ordering (Appendix 5).

We calculate detection events for a 40 kt liquid argon detector, representing the under-construction Deep Underground Neutrino Experiment (DUNE; Abi et al. 2021) capable of detecting large numbers of ν_e from nearby CCSNe (Kato et al. 2017). Table 1 summarizes the different interaction channels: charged-current (CC) reactions on ^{40}Ar by ν_e and $\bar{\nu}_e$; neutral-current (NC) reactions on ^{40}Ar for all flavors; and electron scattering (ES) for all flavors. The ν_eCC reaction channel accounts for approximately 70%–80% of the total counts in our models.

Table 1
Neutrino Detection Channels Used in the SNOWGLOBES Analysis for a DUNE-like Liquid Argon Detector

Channel	Reaction	Flavor	(%)
ν_eCC	$\nu_e + {}^{40}\mathrm{Ar} \rightarrow e^- + {}^{40}\mathrm{K}$	ν_e	70–80
$\bar{\nu}_e$CC	$\bar{\nu}_e + {}^{40}\mathrm{Ar} \rightarrow e^+ + {}^{40}\mathrm{Cl}$	$\bar{\nu}_e$	$\lesssim$1
NC	$\nu + {}^{40}\mathrm{Ar} \rightarrow \nu + {}^{40}\mathrm{Ar}$	ν_e, $\bar{\nu}_e$, ν_x	10–20
ES	$\nu + e^- \rightarrow \nu + e^-$	ν_e, $\bar{\nu}_e$, ν_x	~7

Note. The reaction channels are CC, NC, and ES. Also listed are the rough percentage contributions of each channel to our total counts, which vary by model and choice of flavor mixing.

We capture the neutronization burst by integrating events over 100 ms centered on the bounce, using 5 ms time bins and 0.2 MeV energy bins. For each model and flavor-mixing case, we thus obtain the total neutrino counts and the mean detected neutrino energy, $\langle E \rangle$, summed over all detection channels.

3. Results

Our collection of 612 simulations can be sorted into three groups based on the explosion outcomes for each progenitor. First, there are those models that, for a given progenitor, fail to explode for all three EC rate sets. Second, there are those with mixed explosion outcomes between the rate sets. And third, there are those that successfully explode for all three sets.

Of the 200 progenitors, 126 fail for all three rate sets, 29 have mixed explosion outcomes, and 44 explode for all sets. The 10.25 $M_\odot$ progenitor simulations experience numerical crashes mid-shock revival, and are excluded from discussions of explosion outcome. Of the mixed-outcome group, the IPA models always fail, whereas LMP and LMP+N50 both explode in 26 cases, and LMP+N50 is the only explosion for the remaining three cases (22, 27.4, and 33 $M_\odot$). In summary, there are 44 successful explosions for IPA, 70 for LMP, and 73 for LMP+N50.

The data presented here, and the codes used to analyze it, are publicly available (Appendix 5).

3.1. Reference Progenitors

We here present detailed simulation comparisons for the 12, 20, and 40 $M_\odot$ progenitors. These progenitors are representative of the three groups of explosion outcomes, respectively: all EC rate sets fail to explode; mixed outcomes; and all successfully explode.

The evolution of the shock radius, $r_{\rm sh}$, and the neutrino heating efficiency, $\eta_{\rm heat}$, are shown in Figure 1. Here, $\eta_{\rm heat}$ is the fraction of the total ν_e and $\bar{\nu}_e$ luminosity absorbed in the gain region, which we estimate following O'Connor & Ott (2011). All 12 $M_\odot$ models fail to explode and all 40 $M_\odot$ models successfully explode. For the 20 $M_\odot$ models, the LMP, LMP +N50, and both 10× models explode, whereas the IPA and both 0.01× models fail.

A consistent hierarchy of $r_{\rm sh}$ evolution is seen across the reference progenitors. Overall, the IPA models reach the

[9] https://github.com/evanoconnor/nulib
[10] https://github.com/SNOwGLoBES/snowglobes
[11] www.mpi-hd.mpg.de/personalhomes/globes

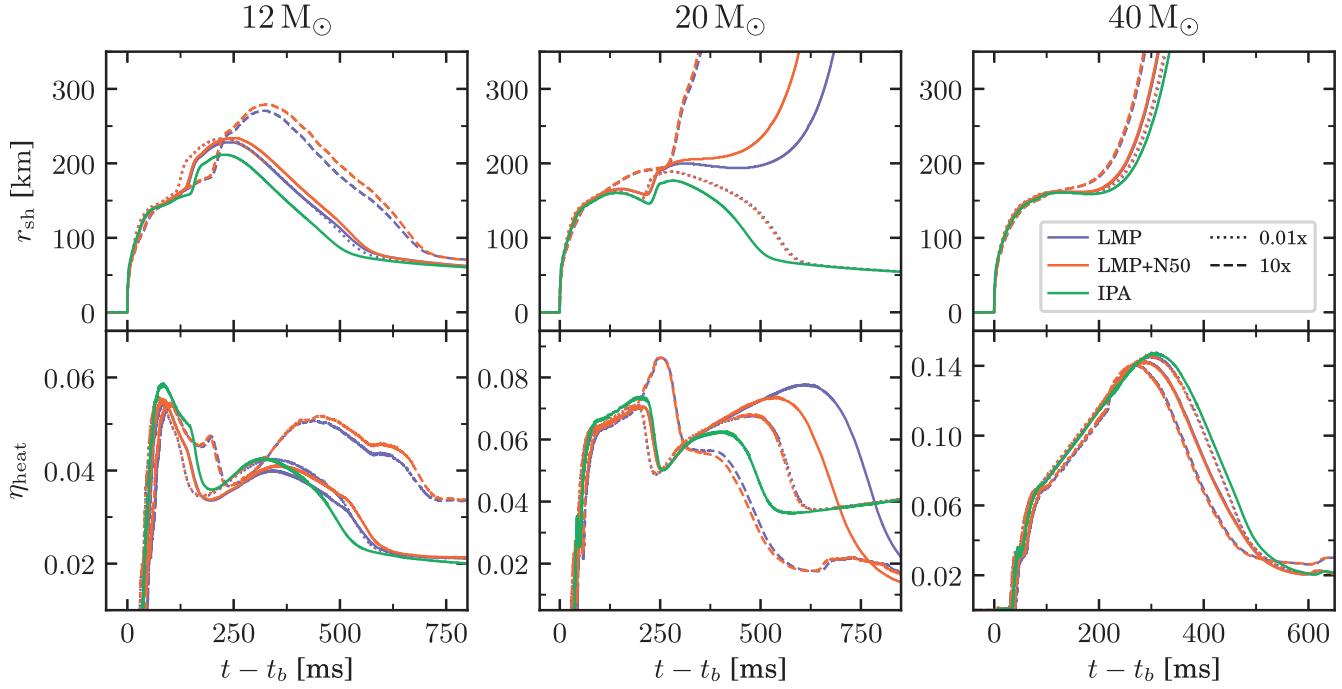

Figure 1. Post-bounce evolution of shock radius (r_{sh}) and neutrino heating efficiency in the gain region (η_{heat}) for three reference progenitors (Section 3.1). The 0.01× and 10× models consist of the LMP and LMP+N50 rates systematically scaled by factors of 0.01 and 10 (Section 2.1). Note the different η_{heat} ranges.

smallest r_{sh}, experience the earliest shock recession (12 and 20 $M_\odot$), and the latest shock revival (40 $M_\odot$), followed closely by the 0.01× models. The LMP and LMP+N50 models reach larger r_{sh} before recession (12 $M_\odot$) and undergo earlier shock revival (20 and 40 $M_\odot$). Finally, the 10× models reach the largest r_{sh} before recession (12 $M_\odot$) and the earliest shock revivals (20 and 40 $M_\odot$).

For the 20 $M_\odot$ progenitor, LMP+50 appears to require a smaller heating efficiency for shock revival than LMP, suggesting more favorable explosion conditions. The 10× models experience a surge in η_{heat} around 250 ms, which appears to contribute to an early shock runaway. In contrast, IPA does not reach sufficient η_{heat} before its shock contracts, shrinking the available gain region for neutrino interactions.

The matter profiles at core bounce are shown in Figure 2 for the 20 $M_\odot$ progenitor (left) and the full set of 200 progenitors (right). We define bounce as the moment when the peak entropy in the core reaches 3 k_B baryon^{-1}. We also define the inner core mass at bounce, M_{core}, as the mass enclosed within this point (also known as the homologous core mass).

As with r_{sh}, the models maintain a consistent hierarchy, even across the entire population of progenitors. The IPA models have the largest inner core mass and electron fraction, entropy, density, and infall velocity. This trend is followed, in order, by the 0.01×, LMP+N50, LMP, and finally 10× models. This ordering is reversed for the Y_e outside the shock, where IPA is the lowest and 10× the largest.

In Figure 3, the lepton fraction is shown versus density at bounce for the 20 $M_\odot$ progenitor. Above the neutrino-trapping densities of $\sim 10^{12}$ g cm^3, the 0.01× models have the largest Y_l, followed by IPA, LMP+N50, LMP, and 10×.

3.2. Population Comparisons

A selection of properties at core bounce for all 200 progenitors are plotted versus the progenitor iron core mass, M_{Fe}, in Figure 4. These quantities in particular demonstrate large differences between the EC rates compared to differences between the progenitors.

The electron fraction of the inner core at bounce, Y_e, is taken at the $M = 0.1\,M_\odot$ enclosed mass coordinate (see also Figure 2). The IPA models have the largest Y_e (i.e., weakest deleptonization), followed by LMP+N50 and LMP.

The extent of deleptonization translates directly into the inner core mass at bounce, M_{core}. The IPA rates produce systematically larger M_{core} than LMP by around 0.08 $M_\odot$ (≈15%), whereas LMP+N50 are around 0.03 $M_\odot$ (≈5%) larger.

The density profile at bounce (Figure 2) determines the gravitational potential at the shock, V_b. Following previous trends, IPA results in a potential around 15% deeper than LMP, compared to LMP+N50, which is consistently ≈5% deeper.

Also shown is t_{ν_e}, the time when the shock crosses the ν_e sphere immediately following the bounce. IPA reaches t_{ν_e} consistently ≈1.5 ms earlier than LMP, while LMP+N50 is ≈0.5 ms earlier. This relatively small but persistent difference impacts the neutrino signal of the deleptonization burst (Section 3.4).

Quantities that have much larger variation between progenitors than between the EC rates are illustrated in Figure 5. For clarity, we emphasize the changes due to EC rates by plotting the fractional or absolute difference relative to LMP for each progenitor. For example, the difference of a given quantity X corresponds to $\Delta X = X - X_{LMP}$. For quantities where the absolute value depends somewhat arbitrarily on the initial conditions, we instead compare the fractional difference, i.e., $\Delta X/X = (X - X_{LMP})/X_{LMP}$.

The time of core bounce from the start of the simulation, t_b, illustrates the speed of collapse from a common starting point. IPA reaches core bounce between 2.5% and 8.5% earlier than LMP (corresponding to approximately 10–17 ms), whereas LMP+N50 reaches bounce $\lesssim$1.5%) later than LMP

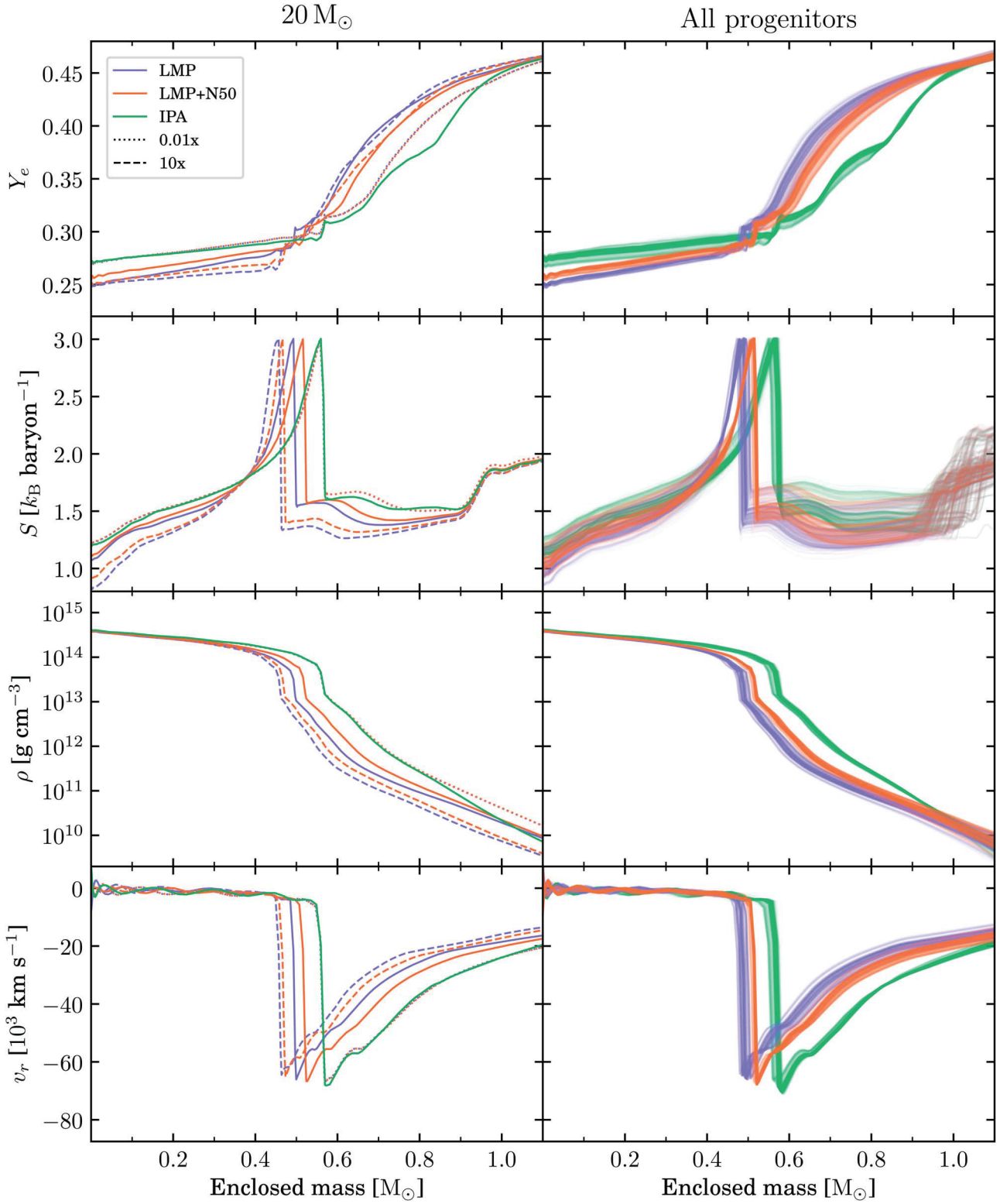

Figure 2. Radial matter profiles at core bounce vs. enclosed mass for the 20 $M_\odot$ progenitor (left), and all 200 progenitors between 9 and 120 $M_\odot$ (right). From top to bottom: electron fraction (Y_e); specific entropy (S); density (ρ); and radial velocity (v_r). Differences between the EC rate are typically larger than differences between the progenitors. For the 20 $M_\odot$ progenitor, the IPA and 0.01× models fail to explode, whereas the LMP, LMP+N50, and 10× models successfully explode (Figure 1).

(corresponding to $\lesssim$2 ms). In both cases, the difference is the smallest for larger progenitor iron core masses.

The mass accretion rate through $r = 500$ km at bounce, $\dot{M}_b$, further illustrates the strength of collapse. Overall, IPA reaches accretion rates around 0.1 $M_\odot$ s^{-1} larger than LMP, whereas LMP+N50 is $\approx$0.1 $M_\odot$ s^{-1} smaller.

The maximum shock radius reached for failed explosions, max(r_{sh}), further supports the differences in shock evolution seen in the reference progenitors (Figure 1). IPA reaches the

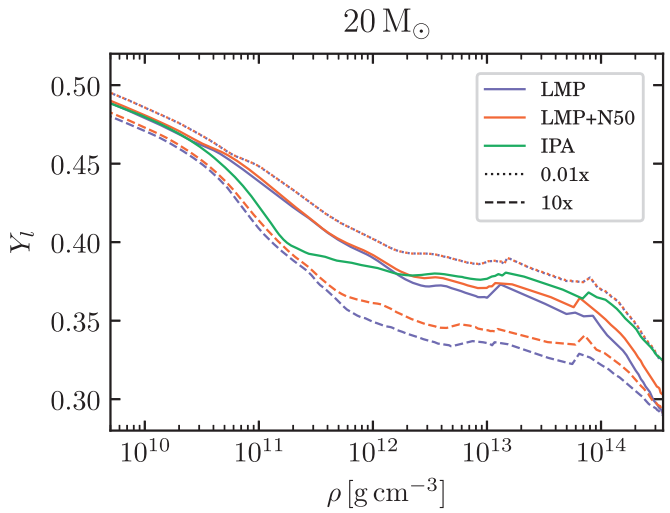

Figure 3. Lepton fraction (Y_l) vs. density (ρ) at core bounce for the 20 $M_\odot$ progenitor. Of the baseline EC rate sets, IPA has the weakest deleptonization at densities $\gtrsim 10^{12}$g cm^3, but the strongest at lower densities.

smallest $r_{\rm sh}$, generally around 5–20 km smaller than LMP, whereas LMP+N50 is around 0–5 km larger.

3.3. Compact Remnants

The compact remnant properties are compared in Figure 6 as the absolute difference relative to LMP, as used in Section 3.2.

The PNS mass at the end of the simulation, $M_{\rm PNS}$, is compared for exploding models. Here, we define $M_{\rm PNS}$ as the baryonic mass contained in the region above a density of 10^{12} g cm^3.

IPA tends to produce a heavier PNS, with progenitors of $M_{\rm Fe} \gtrsim 1.45\,M_\odot$ around 0.02–0.1 $M_\odot$ larger than LMP. On the other hand, LMP+N50 tends to produce a similar or slightly lighter PNS, at most up to 0.01–0.02 $M_\odot$ lighter than LMP. All of the exploding models for $M_{\rm Fe} \lesssim 1.45 M_\odot$ are within 0.02 $M_\odot$ of LMP.

The post-bounce time to BH formation, $t_{\rm BH}$, is compared for the subset of models that reach PNS collapse. Not all failed-explosion models reach PNS collapse within the time simulated (between 1–5 s post-bounce). For the handful of models that do allow comparison with LMP, IPA reaches BH formation around 20–80 ms earlier, whereas LMP+N50 is only around 2–7 ms earlier.

Assuming the entire star is accreted, there would be no difference in the final BH mass between the EC rates.

3.4. Neutrino Signal

The neutrino emission at $r = 500$ km is shown in Figure 7 for the 20 $M_\odot$ progenitor. The three baseline sets reach similar peak electron-neutrino luminosities of $L_{\nu_e} \approx 5 \times 10^{53}$erg s^{-1}. The 0.01× luminosities peak roughly 10% higher, whereas the 10× peak roughly 10% lower. Additionally, the IPA and 0.01× models peak slightly earlier than the LMP, LMP+N50, and 10× models, which have ν_e emission spread out to later times. The mean neutrino energies, $\langle E_\nu \rangle$, follow a similar pattern. The $\bar{\nu}_e$ and ν_x emission is largely reversed, with IPA and 0.01× generally having the largest luminosities and mean energies, followed by LMP+N50, LMP, and 10×.

The predicted neutrino burst signal in a DUNE-like detector is shown for all 612 models across 200 progenitors in Figure 8.

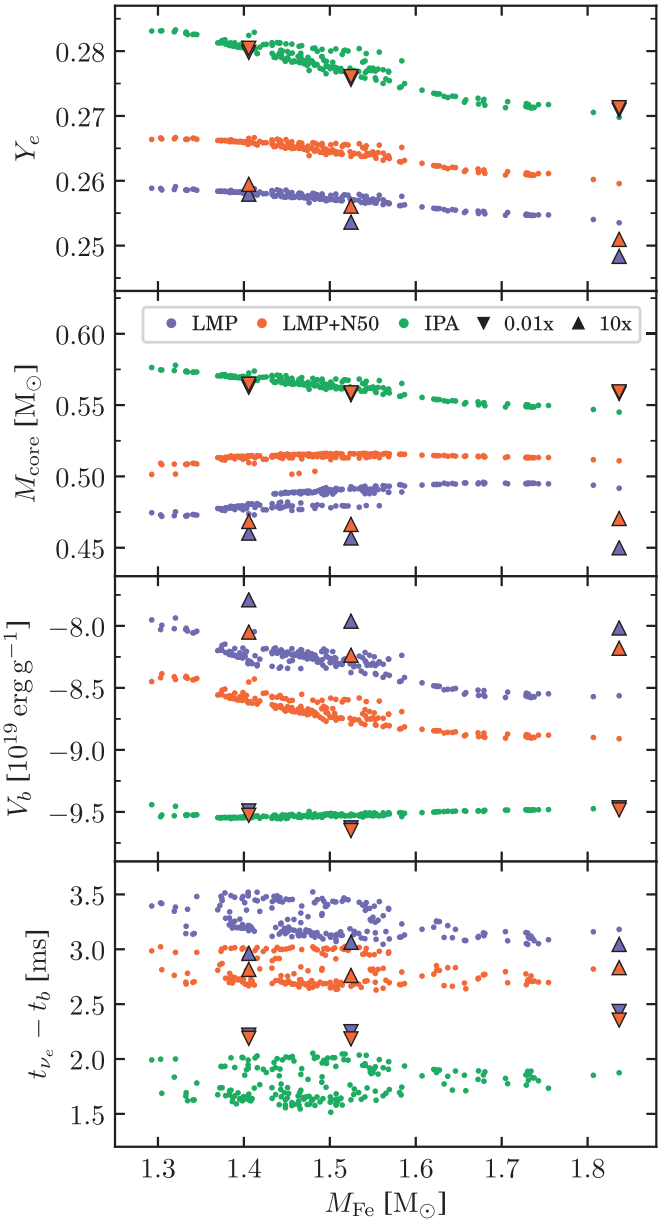

Figure 4. Core bounce properties vs. progenitor iron core mass, $M_{\rm Fe}$, for all simulations (Section 3.2). From top to bottom: electron fraction at bounce in the $M = 0.1\,M_\odot$ mass shell (Y_e); inner core mass at bounce ($M_{\rm core}$); gravitational potential at the shock at bounce (V_b); and convergence time of the shock with the ν_e sphere, relative to bounce ($t_{\nu_e} - t_b$). The 0.01× and 10× rate-scaled models are marked by downward and upward-pointing triangles, respectively (appearing from left to right: 12, 20, and 40 $M_\odot$). In most cases, the differences between EC rates are larger than the dependence on stellar progenitor.

For all three MSW flavor-mixing cases, there are consistent differences in the detected neutrinos between the EC rate sets.

Overall, LMP and LMP+N50 produce similar total neutrino counts and mean detected energies, $\langle E \rangle$, with larger differences for IPA, particularly in $\langle E \rangle$. When no flavor mixing is assumed, IPA results in the lowest counts and $\langle E \rangle$. The effect is reversed when flavor mixing is included for both normal and inverted neutrino mass ordering. Overall, the inclusion of flavor-mixing results in fewer counts and larger $\langle E \rangle$.

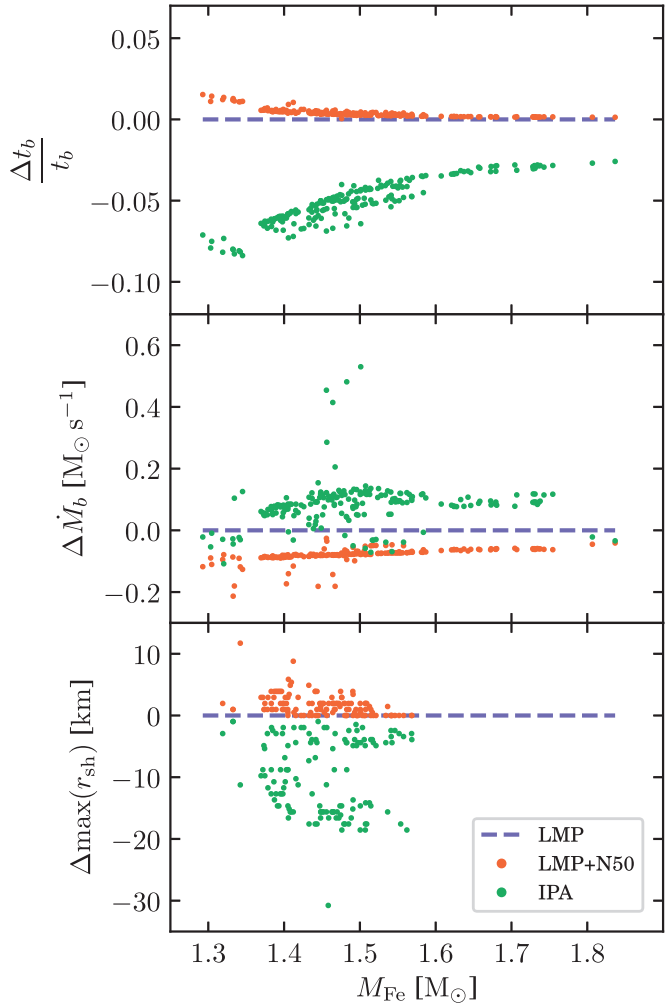

Figure 5. Fractional and absolute differences of LMP+N50 and IPA models relative to LMP vs. progenitor iron core mass (Section 3.2). The quantities compared, from top to bottom: time to bounce from the start of the simulation (t_b); accretion rate through $r = 500$ km at bounce ($\dot{M}_b$); and maximum shock radius reached for failed-explosion models (max(r_{sh})). Note the grid resolution of the simulation limits the precision of r_{sh} here to ≈0.5 km.

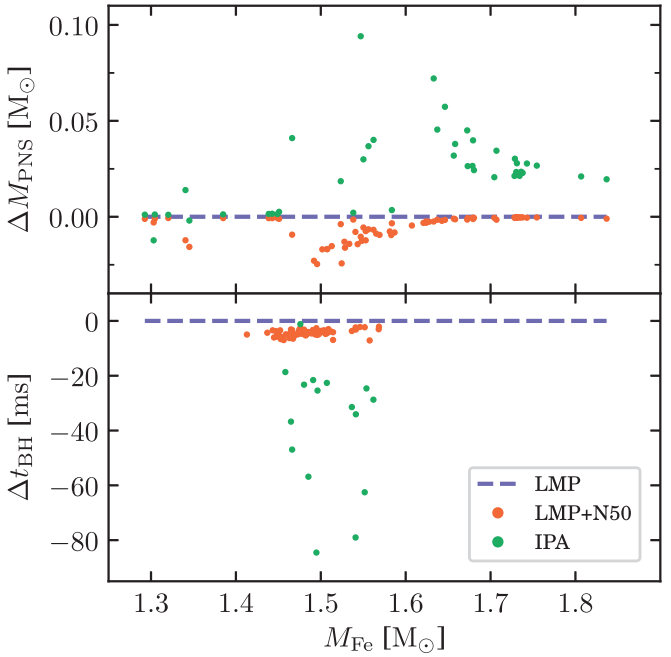

Figure 6. Absolute difference of compact remnant properties relative to LMP (Section 3.3), vs. progenitor iron core mass. Top: PNS mass at the end of the simulation (M_{PNS}) for exploding models. Bottom: time from bounce to BH formation (t_{BH}).

4. Discussion

The choice of EC rates has a clear impact on our simulations of CCSNe. Perhaps the starkest difference in outcome is whether the models undergo successful shock revival and explosion. This variation in outcome can largely be traced to the pre-bounce core-collapse phase, where the EC rates control deleptonization and set the conditions at the core bounce for the subsequent shock evolution. The EC rates also influence the formation of the compact remnant and the observable neutrino signals.

4.1. Collapse and Bounce

Due to the lack in IPA of forbidden transitions and thermal unblocking effects, the rates are limited to EC on free protons when the average nucleus has a neutron number of $N \geqslant 40$ (Hix et al. 2003). Because protons are less abundant than neutron-rich nuclei at high densities, the total number of ECs is suppressed, resulting in a larger Y_e in the inner core at bounce compared to LMP and LMP+N50, which do allow EC for $N \geqslant 40$. On the other hand, ECs are actually enhanced in IPA at low densities below the $N = 40$ threshold because the rates are overestimated compared to the LMP-based tables (Lentz et al. 2012).

The combined effect is a larger Y_e and Y_l for IPA in the inner core region ($\rho \gtrsim 10^{12}$ g cm^3) and lower values in the outer core compared to LMP and LMP+N50 (Figures 2 and 3). This enhanced deleptonization of matter passing through lower densities accelerates the collapse to core bounce, leading to stronger accretion rates, larger infall velocities, larger inner core mass, deeper gravitational potential, and higher densities (Figures 4 and 5).

These bounce profile differences between the IPA and LMP-based rates are well-established in the literature, noted by Langanke et al. (2003) and Hix et al. (2003), and reproduced in subsequent studies (e.g., Lentz et al. 2012; Sullivan et al. 2016; Richers et al. 2017; Pascal et al. 2020).

4.2. Shock Evolution and Explosion Outcome

Initially, owing to the larger inner core mass, the IPA shock has more kinetic energy and less overlying material to pass through than LMP and LMP+N50. Competing with these favorable conditions, however, are the higher densities (and thus deeper gravitational potential), faster infall of the overlying material (Figures 2 and 4), and stronger neutrino cooling. Despite rapid expansion at early times in IPA, the shock is soon overwhelmed by accretion and neutrino cooling, leading to earlier stalling at smaller radii (Figure 5). Compounded by the smaller gain region now available for neutrino heating, the result is an earlier shock recession or a delayed explosion (Figure 1). By contrast, LMP+N50 tends to have more favorable conditions for a successful explosion, with the slowest collapse to bounce and smallest accretion rates (Figure 5).

The impact of the EC rates on shock evolution is borne out by the incidence of successful explosions. Of the 73 progenitors with at least one explosion among the EC rate

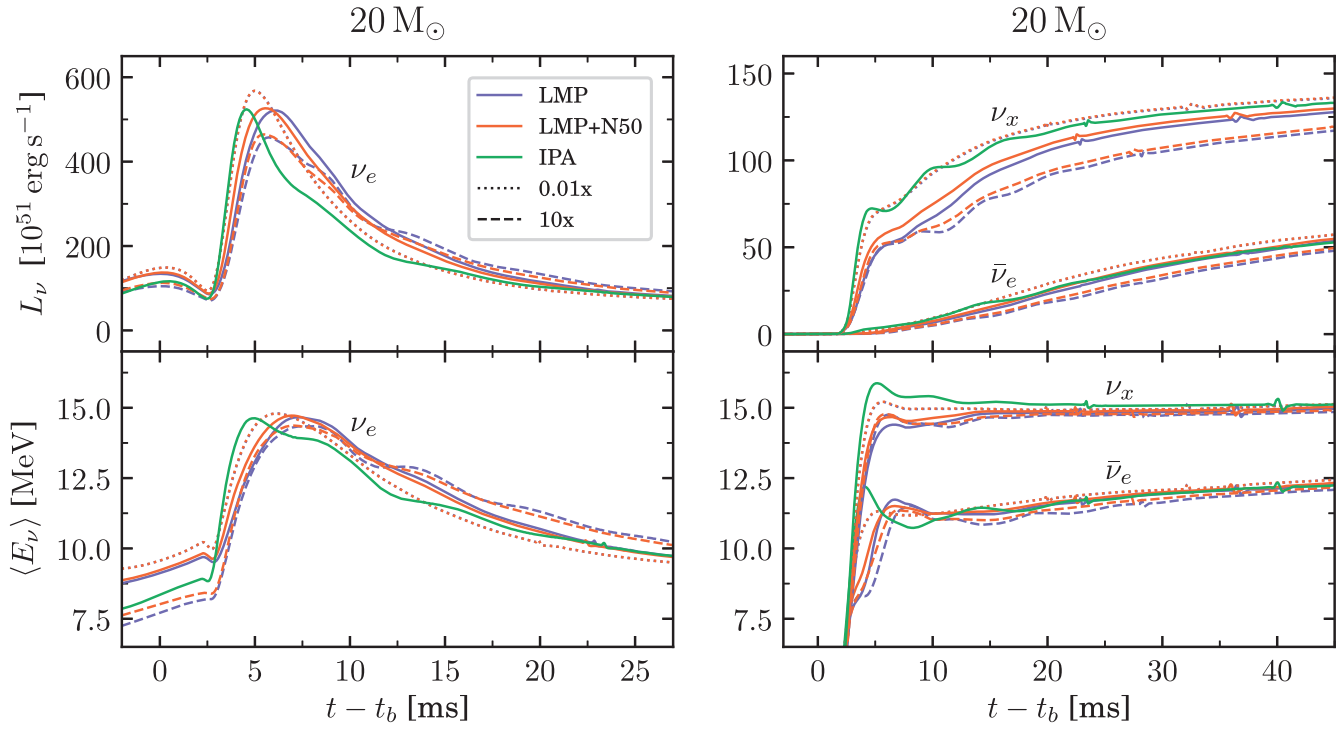

Figure 7. Neutrino emission at $r = 500$ km for the 20 $M_\odot$ progenitor. Top row: neutrino luminosity, L_ν. Bottom row: mean neutrino energy, $\langle E_\nu \rangle$. Left: electron-neutrino (ν_e) emission. Right: electron antineutrino ($\bar{\nu}_e$) and heavy-lepton neutrino (ν_x) emission. Note the different time and L_ν ranges.

sets, LMP+N50 explodes in all 73 and LMP explodes in 70. In contrast, IPA explodes in only 43 of these cases, and for no progenitor is IPA the sole explosion.

4.3. Compact Remnants

The EC rates also impact the formation of the compact remnant (Section 3.3). In successful explosions, the PNS mass, $M_{\rm PNS}$, is effectively determined by the total mass accreted through the shock before shock revival unbinds the remaining material. The two deciding factors are thus the accretion rate and the elapsed time before shock runaway. IPA typically experiences both higher accretion rates (Figure 5) and later shock revival (Figure 1), resulting in the largest $M_{\rm PNS}$ (Figure 6). The converse effects on LMP+N50 result in smaller $M_{\rm PNS}$.

In the case of failed explosions, the conditions at core bounce influence the evolution and eventual collapse of the PNS. The larger core Y_e and $M_{\rm core}$ in IPA results in a stronger initial shock, producing a larger PNS radius and stronger ν_x radiation (Figure 7). The subsequent cooling of the PNS results in IPA reaching collapse approximately 20–80 ms earlier than LMP (Figure 6). LMP+N50 has only marginally more efficient PNS cooling than LMP, and collapses at most a few milliseconds earlier. A change in the BH formation time would alter the shutoff of multimessenger signals from neutrinos and gravitational waves.

4.4. Neutrino Emission

The effects of EC on deleptonization and shock formation also manifest in the neutrino emission around bounce (Section 3.4). For IPA, a larger $M_{\rm core}$ at bounce and stronger initial shock, combined with smaller neutrino spheres due to lowered opacities, leads to a faster convergence of the shock with the ν_e sphere, producing an earlier peak in L_{ν_e} (Figure 7). The mean time between core bounce and the shock reaching the ν_e sphere was 1.8 ± 0.1 ms for IPA, 3.3 ± 0.1 ms for LMP, and 2.8 ± 0.1 ms for LMP+N50 (1σ standard deviations; Figure 4). These differences in L_{ν_e} have been noted in previous EC rate studies (e.g., Hix et al. 2003; Lentz et al. 2012; Sullivan et al. 2016; Pascal et al. 2020).

For LMP and LMP+N50, the extended emission of ν_e at larger L_{ν_e} and $\langle E_{\nu_e} \rangle$ results in higher detected neutrino counts and energies in a DUNE-like liquid argon detector when no flavor mixing is assumed (Figure 8).

When MSW flavor mixing is included with normal neutrino mass ordering, approximately 98% of the emitted ν_e are converted to ν_x, and vice versa. This reduces the number of ν_e available for detection in the dominant ν_eCC channel (Table 1), resulting in fewer total counts. There is also a shift to larger $\langle E \rangle$ because most of the ν_e that are now detected originate as high-energy ν_x. Because IPA has larger emitted L_{ν_x} and $\langle E_{\nu_x} \rangle$, it now has the highest counts and $\langle E \rangle$.

The inverted mass ordering case is somewhat intermediate, with only 70% of the emitted ν_e converted to ν_x, and vice versa. These favorable survival probabilities result in overall counts and $\langle E \rangle$ that are between the previous two cases. This appears to roughly coincide with the *crossover* point, where all three EC rates produce very similar counts.

The large error bars from Poisson statistics alone suggest that these differences would be difficult to detect under these narrow assumptions, especially for $\langle E \rangle$, even if the progenitor was known. Additionally, there are degeneracies between the EC rate and the impacts of the progenitor star, neutrino mass hierarchy, and potentially the nuclear EOS (not investigated here). Reducing the uncertainties via larger count numbers could be achieved by combining measurements from multiple neutrino detectors, or if the supernova occurred closer than the assumed 10 kpc. The degenerate signals might be broken by incorporating into the analysis: additional parts of the neutrino

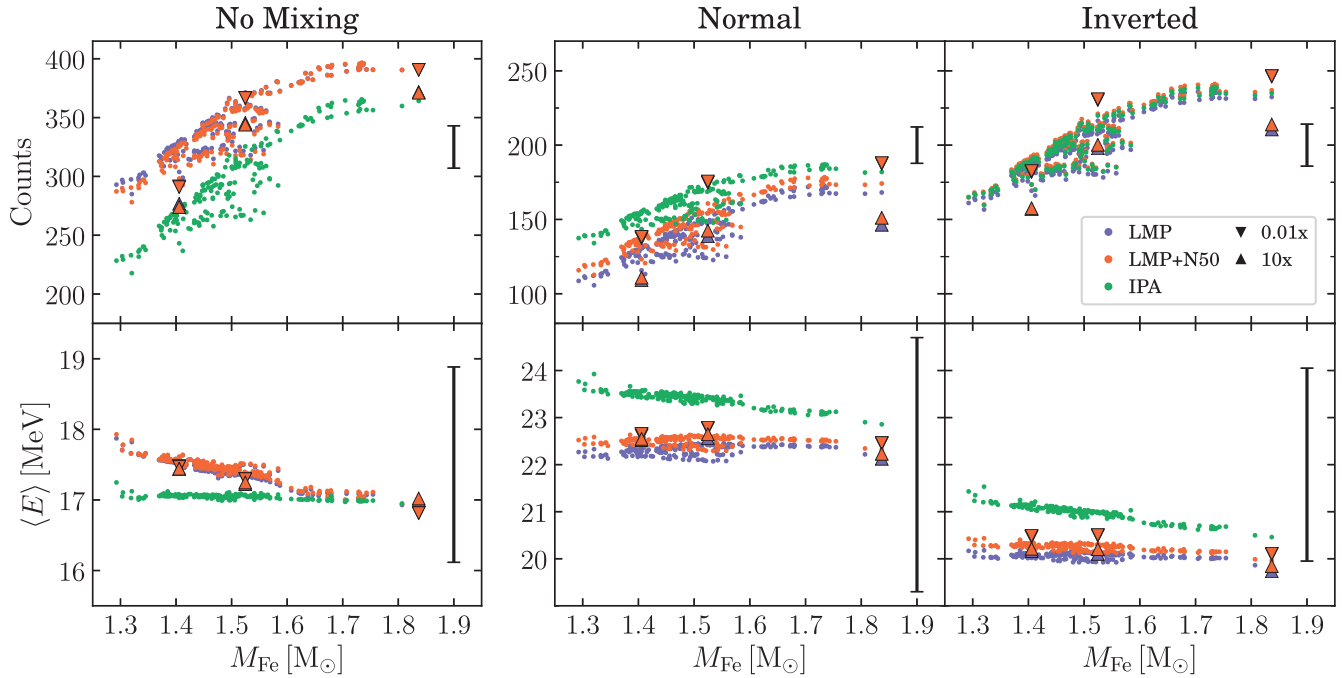

Figure 8. Neutrino burst signal in a DUNE-like liquid argon detector for all 200 progenitors, vs. progenitor iron core mass. Top row: total neutrino counts. Bottom row: mean detected neutrino energy. From left to right are the adiabatic flavor-mixing implementations: no flavor mixing, normal mass ordering, and inverted mass ordering. The signal is integrated over 100 ms centered on the bounce (Section 2.3), across all detection channels (Table 1), and assuming a distance of 10 kpc. The error bars show typical 1σ uncertainties due to Poisson counting statistics alone. Note the different y-axis ranges.

light curve (e.g., Segerlund et al. 2021); additional detectors sensitive to other neutrino flavors (e.g., water Cherenkov detectors); or, given sufficient counts, the full neutrino spectrum instead of an average energy.

5. Conclusion

We have produced a suite of 612 one-dimensional CCSN simulations, using three sets of EC rates and 200 stellar progenitors between 9 and 120 $M_\odot$.

The three EC rate sets were (Section 2.1): an IPA (Bruenn 1985); a microphysical library with parametrized rates in the high-sensitivity $N = 50$ region (LMP; Sullivan et al. 2016; Titus et al. 2018); and the same library with updated $N = 50$ rates (LMP+N50; Titus et al. 2019).

Of the 200 progenitors, there were 43 successful explosions for the IPA set, 70 for LMP, and 73 for LMP+N50. In general, the IPA models reached smaller shock radii and exploded later than their LMP and LMP+N50 counterparts (Section 3.1). Of the latter two, LMP+N50 appeared marginally more favorable to explosion, with larger shock radii and earlier shock runaway than LMP.

At core bounce, IPA typically had the largest inner core mass, electron fraction, density, accretion rate, infall velocity, and gravitational potential (Figures 2, 4, and 5). The next largest values were generally LMP+N50 followed by LMP, although LMP+N50 changed places with LMP for the collapse time and accretion rate (Figure 5). The standard ordering was also reversed for Y_e in the outer core, where IPA had the lowest values and LMP the highest (Figure 3).

For exploding progenitors, IPA produced a PNS mass around 0.02–0.1 $M_\odot$ larger than LMP due to higher accretion rates and delayed shock revival, and LMP+N50 was typically $\lesssim 0.02\,M_\odot$ smaller (Figure 6). For failed explosions, enhanced PNS cooling in IPA resulted in a collapse to BH roughly 20–80 ms earlier than LMP, whereas LMP+N50 was at most a few milliseconds earlier.

Without flavor mixing, the extended ν_e emission of LMP and LMP+N50 following bounce (Figure 7) resulted in higher detected counts and mean energies than IPA in a DUNE-like liquid argon detector (Figure 8). Conversely, when adiabatic flavor mixing is included, the enhanced ν_x emission in IPA is converted to ν_e, resulting in higher counts and energies than LMP and LMP+N50. Given only $\sim 10^2$ counts, however, these differences were typically smaller than the estimated uncertainties.

All of these results largely stem from the total rate of ECs at different densities during collapse (Section 4.1). For IPA, the total EC rate is overestimated at lower densities, but subsequently underestimated at higher densities due to Pauli blocking on a mean nucleus of $N \geqslant 40$. The LMP-based rates unblock EC for neutron-rich nuclei, and so deleptonization proceeds further than IPA during collapse. The updated $N = 50$ rates in LMP+N50 are lower than the parametrized rates in LMP, producing an intermediate case between LMP and IPA (Figure 4).

It is important to emphasize the limitations of our study. While our STIR framework (Couch et al. 2020) approximates the effects of turbulence in 1D, there is ultimately no substitute for multidimensional simulations. Only high-fidelity 3D simulations can hope to fully capture the interplay between fluid instabilities, magnetohydrodynamics, and neutrino transport in CCSNe (e.g., Hanke et al. 2013; Lentz et al. 2015; O'Connor & Couch 2018; Summa et al. 2018; Müller et al. 2019). Our progenitors from Sukhbold et al. (2016) were 1D, solar-metallicity, nonrotating, and nonmagnetic, and do not represent the full variety of stellar populations. The progenitor models also used microphysical EC rates, and so the sudden transition to approximate rates in our IPA models is somewhat artificial. Although we accounted for adiabatic flavor mixing

when calculating neutrino signals, there remains copious uncertainty around the effects of flavor oscillations, which were not included in our simulations.

We note that our study only considered the SFHo nuclear EOS, as previous works have demonstrated that the EOS dependence of the collapse and early post-bounce phase ($\lesssim$100 ms) is dwarfed by the impact of EC rate uncertainties (Sullivan et al. 2016). We posit that the qualitative differences seen here between the EC rates beyond ≈100 ms post-bounce are unlikely to be dramatically altered by the EOS. Nevertheless, the choice of EOS can alter the nuclear abundances that EC acts upon (Nagakura et al. 2019), and it would be valuable to test our assumption in a future study.

Finally, the updated rates in LMP+N50 do not include temperature dependence effects (Dzhioev et al. 2020). Very recently, Giraud et al. (2022) reported new finite-temperature calculations for the $N = 50$ region, with rates around an order of magnitude higher than LMP+N50 and about a factor of 5 below the LMP rates. Their simulations suggest that CCSN properties would be intermediate between the LMP and LMP +N50 models presented here, which are already in relatively good agreement compared to the commonly used IPA rates. Work is underway to incorporate these new rates into NULIB so that they can be freely used in future CCSN simulations.

EC plays a central role in deleptonization, shock formation, and neutrino production during core collapse. Our study has explored the effects of updated EC rates in the high-sensitivity $N = 50$ region, including a detailed comparison between microphysical rates and a simple IPA. By producing simulations across 200 progenitors, we have shown there are clear, systematic impacts of EC rates on the core structure, shock dynamics, and neutrino signals throughout the CCSNe mechanism.

This work was supported in part by Michigan State University through computational resources provided by the Institute for Cyber-Enabled Research. S.M.C. is supported by the US Department of Energy, Office of Science, Office of Nuclear Physics, under Award Numbers DE-SC0015904 and DE-SC0017955. R.T. and R.Z. are supported by the US National Science Foundation under Grants PHY-1913554 (Windows on the Universe: Nuclear Astrophysics at the NSCL), PHY-1430152 (JINA Center for the Evolution of the Elements), and PHY-1927130 (AccelNet-WOU: International Research Network for Nuclear Astrophysics [IReNA]). E.O.C. is supported by the Swedish Research Council (Project No. 2020-00452).

Software: FLASH [12] (Fryxell et al. 2000; Dubey et al. 2009), NSCL Weak-rate Library v1.2 (Sullivan 2015), NULIB (O'Connor 2015), SNOWGLOBES (Scholberg 2012), GLOBES (Huber et al. 2005), MATPLOTLIB [13] (Hunter 2007), NUMPY [14] (Harris et al. 2020), SCIPY[15] (Virtanen et al. 2020), YT[16] (Turk et al. 2011), PANDAS[17] (Pandas development team et al. 2022), XARRAY[18] (Hoyer & Hamman 2017; Hoyer et al. 2020), ASTROPY[19] (Astropy Collaboration et al. 2013, 2018), FLASHBANG [20] (Johnston 2022a), FLASH_SNOWGLOBES[21] (Johnston 2022b).

[12] https://flash.rochester.edu/site/
[13] https://matplotlib.org
[14] https://www.numpy.org
[15] https://www.scipy.org
[16] https://yt-project.org
[17] https://pandas.pydata.org
[18] https://xarray.pydata.org

Data Availability

The data for all simulations presented in this work are publicly available in a Mendeley Data repository (Johnston et al. 2022). The data set includes summarized simulation results, radial profiles at core bounce, time-dependent quantities (e.g., shock radius and neutrino luminosities), and time-binned SNOWGLOBES neutrino counts and energies.

Much of the model analysis and plotting were performed using our publicly available PYTHON package FLASHBANG (Johnston 2022a).

Neutrino Flavor Mixing

When calculating detectable neutrino counts with SNOWGLOBES (Section 2.3), we account for adiabatic neutrino flavor conversions due to MSW matter effects (Dighe & Smirnov 2000). Following similar approaches in Nagakura (2021) and Segerlund et al. (2021), we calculate the neutrino flux at Earth, F_i, for each neutrino flavor i, using

$$F_e = pF_e^0 + (1-p)F_x^0, \tag{A1}$$

$$\bar{F}_e = \bar{p}\bar{F}_e^0 + (1-\bar{p})\bar{F}_x^0, \tag{A2}$$

$$F_x = \frac{1}{2}(1-p)F_e^0 + \frac{1}{2}(1+p)F_x^0, \tag{A3}$$

$$\bar{F}_x = \frac{1}{2}(1-\bar{p})\bar{F}_e^0 + \frac{1}{2}(1+\bar{p})\bar{F}_x^0, \tag{A4}$$

where p and $\bar{p}$ are the survival probabilities, and F_i^0 are the emitted fluxes for each flavor i. Under normal neutrino mass ordering, the survival probabilities are given by

$$p = \sin^2\theta_{13} \approx 0.02, \tag{A5}$$

$$\bar{p} = \cos^2\theta_{12}\cos^2\theta_{13} \approx 0.69, \tag{A6}$$

and under inverted mass ordering by

$$p = \sin^2\theta_{12}\cos^2\theta_{13} \approx 0.29 \tag{A7}$$

$$\bar{p} = \sin^2\theta_{13} \approx 0.02, \tag{A8}$$

where we use mixing parameters of $\sin^2\theta_{12} = 0.297$ and $\sin^2\theta_{13} = 0.0215$ (Capozzi et al. 2017). The no-mixing case is equivalent to $p = \bar{p} = 1$. Note that our simulations use the combined heavy-lepton species $\nu_x = \{\nu_\mu, \nu_\tau, \bar{\nu}_\mu, \bar{\nu}_\tau\}$, and thus we assume

$$F_x^0 = \bar{F}_x^0 \propto \frac{1}{4}L_{\nu_x}, \tag{A9}$$

where L_{ν_x} is the heavy-lepton neutrino luminosity from the simulation (Figure 7). The separated heavy-flavor inputs to SNOWGLOBES are then

$$F_\mu = F_\tau = F_x, \tag{A10}$$

$$\bar{F}_\mu = \bar{F}_\tau = \bar{F}_x. \tag{A11}$$

[19] https://www.astropy.org
[20] https://github.com/zacjohnston/flashbang
[21] https://github.com/zacjohnston/flash_snowglobes

The code used for these calculations is publicly available as a PYTHON package, FLASH_SNOWGLOBES (Johnston 2022b).

ORCID iDs

Zac Johnston https://orcid.org/0000-0003-4023-4488
Sheldon Wasik https://orcid.org/0000-0001-9213-0117
MacKenzie L. Warren https://orcid.org/0000-0001-9440-6017
Evan P. O'Connor https://orcid.org/0000-0002-8228-796X
Remco Zegers https://orcid.org/0000-0001-6076-5898
Sean M. Couch https://orcid.org/0000-0002-5080-5996

References

Abi, B., Acciarri, R., Acero, M. A., et al. 2021, EPJC, 81, 423
Astropy Collaboration, Robitaille, T. P., Tollerud, E. J., et al. 2013, A&A, 558, A33
Astropy Collaboration, Price-Whelan, A. M., Sipőcz, B. M., et al. 2018, AJ, 156, 123
Bruenn, S. W. 1985, ApJS, 58, 771
Burrows, A., Reddy, S., & Thompson, T. A. 2006, NuPhA, 777, 356
Capozzi, F., Di Valentino, E., Lisi, E., et al. 2017, PhRvD, 95, 096014
Couch, S. M., Warren, M. L., & O'Connor, E. P. 2020, ApJ, 890, 127
Dighe, A. S., & Smirnov, A. Y. 2000, PhRvD, 62, 033007
Dubey, A., Antypas, K., Ganapathy, M. K., et al. 2009, ParC, 35, 512
Dzhioev, A. A., Langanke, K., Martínez-Pinedo, G., Vdovin, A. I., & Stoyanov, C. 2020, PhRvC, 101, 025805
Fryxell, B., Olson, K., Ricker, P., et al. 2000, ApJS, 131, 273
Fuller, G. M., Fowler, W. A., & Newman, M. J. 1982, ApJ, 252, 715
Giraud, S., Zegers, R. G. T., Brown, B. A., et al. 2022, PhRvC, 105, 055801
Hanke, F., Müller, B., Wongwathanarat, A., Marek, A., & Janka, H.-T. 2013, ApJ, 770, 66
Harris, C. R., Millman, K. J., van der Walt, S. J., et al. 2020, Natur, 585, 357
Hix, W. R., Messer, O. E., Mezzacappa, A., et al. 2003, PhRvL, 91, 201102
Horowitz, C. J. 2002, PhRvD, 65, 043001
Horowitz, C. J., Caballero, O. L., Lin, Z., O'Connor, E., & Schwenk, A. 2017, PhRvC, 95, 025801
Hoyer, S., & Hamman, J. 2017, JORS, 5
Hoyer, S., Hamman, J., Roos, M., et al. 2020, pydata/xarray v0.15.0, Zenodo, doi:10.5281/zenodo.3631851
Huber, P., Lindner, M., & Winter, W. 2005, CoPhC, 167, 195
Hunter, J. D. 2007, CSE, 9, 90
Janka, H., Langanke, K., Marek, A., Martínezpinedo, G., & Müller, B. 2007, PhR, 442, 38
Johnston, Z. 2022a, flashbang, Zenodo, doi:10.5281/zenodo.6000257
Johnston, Z. 2022b, flash_snowglobes Zenodo, doi:10.5281/zenodo.6012564
Johnston, Z., Wasik, S., Titus, R., et al. 2022, Mendeley Data: 1D Core-collapse Supernova Simulations with Updated N=50 Electron Capture Rates doi:10.17632/w36ns2t3rd.2
Kato, C., Nagakura, H., Furusawa, S., et al. 2017, ApJ, 848, 48
Keil, M. T., Raffelt, G. G., & Janka, H.-T. 2003, ApJ, 590, 971
Langanke, K., & Martınez-Pinedo, G. 2000, NuPhA, 673, 481
Langanke, K., & Martínez-Pinedo, G. 2003, RvMP, 75, 819
Langanke, K., Martínez-Pinedo, G., & Zegers, R. G. T. 2021, RPPh, 84, 066301
Langanke, K., Martínez-Pinedo, G., Sampaio, J. M., et al. 2003, PhRvL, 90, 241102
Lentz, E. J., Mezzacappa, A., Messer, O. E. B., Hix, W. R., & Bruenn, S. W. 2012, ApJ, 760, 94
Lentz, E. J., Bruenn, S. W., Hix, W. R., et al. 2015, ApJL, 807, L31
Marek, A., Dimmelmeier, H., Janka, H.-T., Müller, E., & Buras, R. 2006, A&A, 445, 273
Müller, B., Tauris, T. M., Heger, A., et al. 2019, MNRAS, 484, 3307
Müller, B. 2020, LRCA, 6, 3
Nagakura, H. 2021, MNRAS, 500, 319
Nagakura, H., Furusawa, S., Togashi, H., et al. 2019, ApJS, 240, 38
O'Connor, E. 2015, ApJS, 219, 24
O'Connor, E., & Ott, C. D. 2011, ApJ, 730, 70
O'Connor, E. P., & Couch, S. M. 2018, ApJ, 865, 81
Oda, T., Hino, M., Muto, K., Takahara, M., & Sato, K. 1994, ADNDT, 56, 231
O'Connor, E., Horowitz, C. J., Lin, Z., & Couch, S. 2017, in Supernova 1987A:30 years later - Cosmic Rays and Nuclei from Supernovae and their aftermaths, IAU Symp. S331 (Cambridge: Cambridge Univ. Press), 107
Pandas Development Team, Reback, J., jbrockmendel, et al. 2022, pandas-dev/pandas: Pandas v1.4.2, Zenodo, doi:10.5281/zenodo.3509134
Pascal, A., Giraud, S., Fantina, A. F., et al. 2020, PhRvC, 101, 015803
Pruet, J., Woosley, S. E., & Hoffman, R. D. 2003, ApJ, 586, 1254
Raduta, A. R., Gulminelli, F., & Oertel, M. 2017, PhRvC, 95, 025805
Richers, S., Nagakura, H., Ott, C. D., et al. 2017, ApJ, 847, 133
Scholberg, K. 2012, ARNPS, 62, 81
Segerlund, M., O'Sullivan, E., & O'Connor, E. 2021, arXiv:2101.10624
Steiner, A. W., Hempel, M., & Fischer, T. 2013, ApJ, 774, 17
Sukhbold, T., Ertl, T., Woosley, S. E., Brown, J. M., & Janka, H. T. 2016, ApJ, 821, 38
Sullivan, C. 2015, weakrates: Weak-rate library (ApJ release) Zenodo, doi:10.5281/zenodo.33788
Sullivan, C., O'Connor, E., Zegers, R. G. T., Grubb, T., & Austin, S. M. 2016, ApJ, 816, 44
Summa, A., Janka, H.-T., Melson, T., & Marek, A. 2018, ApJ, 852, 28
Suzuki, T., Toki, H., & Nomoto, K. 2016, ApJ, 817, 163
Titus, R., Ney, E. M., Zegers, R. G. T., et al. 2019, PhRvC, 100, 045805
Titus, R., Sullivan, C., Zegers, R. G. T., Brown, B. A., & Gao, B. 2018, JPhG, 45, 014004
Turk, M. J., Smith, B. D., Oishi, J. S., et al. 2011, ApJS, 192, 9
Virtanen, P., Gommers, R., Oliphant, T. E., et al. 2020, NatMe, 17, 261
Warren, M. L., Couch, S. M., O'Connor, E. P., & Morozova, V. 2020, ApJ, 898, 139